



Effect of shaped laser beam profiles on melt flow dynamics in conduction mode welding

S.M.A. Noori Rahim Abadi^a, Y. Mi^a, F. Sikström^a, A. Ancona^{a,b}, I. Choquet^{a,*}

^a Department of Engineering Science, University West, 461 86, Trollhättan, Sweden

^b CNR-IFN, Institute for Photonics and Nanotechnologies, Physics Department, Via Amendola 173, 70126, Bari, Italy

ARTICLE INFO

Keywords:

Laser beam welding
Beam shaping
Phase change
Melt flow
Free surface deformation

ABSTRACT

A computational fluid dynamics approach is used to analyse the influence of beam shaping in fusion welding on melt thermal flow. Three beam shapes are studied at several welding travel speeds: a reference Gaussian profile and its elliptic elongations along and transverse to the welding travel direction. It is found that these beam shapes change not only the intensity and direction of the melt thermocapillary flow but also the flow pattern. For instance, and contrary to the other profiles, the beam shape elongated along the welding travel direction generates melt front vortices that assist metal pre-heating. It can result in deeper penetration, larger melt volume, and lower amount of thermal energy diffused into the heat affected zone. The simple elongation of a beam profile has thus a non-linear effect on the melt flow and in turn on the seam geometry as well as the temperature gradients in the heat affected zone.

1. Introduction

Laser beam heat sources used in fusion welding enable non-contact operation, precise working with tightly focused heat input, handling complicated joint geometries, and in general short post-process operation times. Gladush and Smurov [1] reported the physics of laser beam processing, including the cause-and-effect relations when applied to fusion welding. Three operation modes are successively observed when increasing the power density: the conduction mode, the transition mode, and the keyhole mode. The keyhole mode, identified by intense vaporisation, generates a narrow heat affected zone and low thermal distortion. The transition mode, characterized by Assuncao et al. [2], has distinctive low rate of increase of the bead depth-to-width ratio due to moderate metal vaporisation that rises with the laser power density. It results in weld seams combining keyhole and conduction mode features. The conduction mode, applied in this study, causes negligible vaporisation. It leads to minor loss in alloying elements that contribute to good mechanical properties, and usually high process stability combined with low level of porosity and spatter.

The laser heat sources used in welding have also several drawbacks. Today their wavelength is commonly of the order of 1 μm so that the beam can be transported from the laser source through an optical fibre to ease process automation. Downstream the fibre, the emitted laser spot

in a section normal to the beam axis is then, in principle, axi-symmetric. Victor [3] did illustrate that this circular shape is not always suited to produce the desired seam geometry, as it can result in e.g. sharp toe angles. Heralic [4] did observe that when a filler wire is fed into the laser beam for welding (or additive manufacturing) the wire often obscures the beam and shadows part of the workpiece in the interaction zone; this shadow effect can result in process instability. Another example of drawback described by Hansen et al. [5] arises in butt joint welding since the gap between the pieces to be welded typically presents some variations in width. Combined with robotized manipulation and the narrow laser beam width, this situation can lead to the formation of weld defects, typically lack of side wall fusion and insufficient weld strength.

Laser beam shaping is being actively investigated to improve process stability and seam geometry through acting on the beam spot area, or shape, or power density distribution, or on combinations of these parameters. It can be realized through tilting the beam as applied by Kumar et al. [6] to study the influence of the beam incidence angle on butt joints welded in keyhole mode. It can also be accomplished defocusing the beam spot as made by Kuryntsev et al. [7] to investigate the effect on the re-crystallization direction at the free surface of the mushy zone. Beam shaping tools permit extending further the variety of beam spot power density distributions. Victor [3] did review the first developments made in welding with beam shaping for tailoring the weld

* Corresponding author.

E-mail addresses: ali.abadi@hv.se (S.M.A. Noori Rahim Abadi), isabelle.choquet@hv.se (I. Choquet).

seam geometry. He designed a custom multi-spectral zinc sulfide beam shaping optic to improve the seam surface in-process through welding with two- and three-spot beam profiles. In a recent study Li et al. [8] did also investigate welding with laser beam shaping for tailoring the microstructure. A variety of beam shaping approaches already exist, ranging from dedicated systems such as the above mentioned multi-spot optic customized through experimental trials by Victor [3] to smooth toe angles, to adaptive techniques like the numerically designed system developed by Tsai and Wu [9] for producing beam shapes with a user-defined irradiance pattern. However, a remaining key difficulty is to conceive profiles with suited outcome. This requires understanding the effect of the beam shape on the welding process stability and the resulting seam quality.

Recently Ayoola et al. [10] studied experimentally the effect of elongating a beam spot shape along various directions by tilting the processing laser. The elongation resulted in Gaussian-elliptic profiles with major to minor axis ratio of about 1.4, and the same energy density distribution apart from the orientation. In particular, they analysed that utilizing the transverse and longitudinal Gaussian-elliptic spot profiles resulted in increased/decreased seam width and depth that balanced each other. They inferred from the principle of energy conservation that the melt pool volume should be kept unchanged when changing the spot orientation. This conjecture assumes implicitly that the heat convection pattern in the melt pool is very similar (apart from being rotated) when transverse and longitudinal Gaussian-elliptic spot profiles are applied. As melt pool volume was not accessible to experimental observation, this presumption remains to be confirmed.

Rasch et al. [11] used diffractive optical elements (DOE) to study the following laser spot profiles: a line, aligned points, and a ring. They noticed a non-linear effect of the beam shape on the geometry of the re-solidification front at the melt tail part, and judged that the rear section was difficult to foresee unless resorting to melt pool simulation or to experimental observation. The ring profile, developed imposing a non-uniform power density distribution to weaken the thermocapillary flow, permits a significant extension of the process window towards a high travel speed. The line and points profiles, both elongated along the travel direction, had the same width and total power density. However, the line profile produced deeper and narrower seam geometry than the points profile. Rasch et al. did attribute these differences in bead geometry to enhanced absorption of the laser beam energy promoted by the presence of a large wave with the line profile. The presence of a wave likely indicate that heat convection was also to some extent different for these two profiles. However the melt flow was not analysed for these two cases.

Sundqvist et al. [12] applied beam shaping with DOE to produce C-shaped joints. They stressed that tailoring the laser beam shape was a complex and tedious task they mainly made experimentally by trial and error. They suggested that it could be supported by numerical models able to predict the effect of the beam shaping on the weld. Such models would provide information not yet accessible to measurement, and process understanding that could reduce the number of experimental trials.

Numerical simulation to support beam shape design and optimisation is still scarce. It was used by Sundqvist et al. [12] solving the heat conduction equation. These authors did conclude that a heat conduction model was too simplified to reproduce sufficiently closely the real melt pool geometry and thus effectively help tailoring the beam shape. They did foresee that the effect of the thermal convection on the seam geometry was a driving physical phenomena important to model. More recently, a thermo-fluid dynamics model was applied by Rasch et al. [11] to supplement experimental observation with calculated melt pool temperature and surface evaporation pressure.

From the above, it is clear that the knowledge on the effect of shaped laser beam profiles on the heat convection through the melt flow dynamic is very limited so far. This understanding is important to be able to design and optimize beam shapes for a specified purpose. Further

investigations are thus needed to develop this understanding. For instance, is the flow pattern in a melt pool kept unchanged (apart from being rotated) when a Gaussian-elliptic spot profile is oriented along different directions? Is the flow pattern different when using a Gaussian profile rather than its elongation along some direction, or is it only the thermocapillary flow that is weakened due to the lowering of the power density? To address these questions a computational fluid dynamics approach is used. The examined test cases are presented in the next section.

2. Problem statement

Three laser beam profiles are investigated in this study. One has a standard circular spot and can be considered as a reference profile. The other profiles are elongated along a specific direction, leading to ellipses. Elliptical spot shapes can be produced through e.g. tilting the beam with respect to the workpiece or using beam oscillations along a suited direction. In this study one elliptical spot is elongated along the travel direction to extend the laser-matter interaction time. The second is elongated along the transverse direction as in butt joints application this is a way to mitigate varying gaps avoiding weld flaws in case of bad joint preparation or fixturing. The three laser beam profiles studied hereafter are denoted

C1: Gaussian-elliptical with major axis along the transverse direction,

C2: Gaussian-elliptical with major axis along the travel direction, and
C3: Gaussian (circular).

It is assumed that for each of these profiles the laser beam is almost at normal incidence. Ongoing research by the authors to develop a new beam shaping technique indeed allows forming spots like C1 and C2 without tilting the beam direction. The related laser power density distributions per unit spot area at time t and in a x,y -plane normal to the beam axis are expressed according to

$$q_{\text{laser}} = \frac{2 \eta P_{\text{laser}}}{\pi r_{\parallel} r_{\perp}} \exp \left[-2 \left(\frac{x - U_{\text{laser}} t}{r_{\parallel}} \right)^2 - 2 \left(\frac{y}{r_{\perp}} \right)^2 \right] \quad (1)$$

where P_{laser} is the laser power, and η the absorption coefficient. The welding travel speed, U_{laser} , is here along the positive x -direction. The two constants r_{\parallel} and r_{\perp} are defined along the welding travel and transverse direction, respectively. They represent half the length of an ellipse minor/major axis and are set according to Table 1. As can be seen in this table the profiles share a common radius. The extent of the deformation along the direction of elongation corresponds to intermediate conditions compared to former studies by Ayoola et al. [10] and by Rasch et al. [11]. The ratio of the major to minor axis is indeed more than twice larger than in Ref. [10], whereas the length to width ratio (for C2) is one third lower than for the line profile of [11]. The same laser power, $P_{\text{laser}} = 1$ kW, is used in all the forthcoming applications. The integrated laser spot power density, $P_d = P_{\text{laser}}/A_{\text{spot}}$ (A_{spot} being the laser beam spot area) is also provided in Table 1.

The three laser beam shapes are applied to conduction mode welding of the Titanium alloy Ti-6Al-4V for the set of welding travel speeds reported in Table 2. Some of the computational results are discussed hereafter as function of the energy density, $E_d = P_d \times t_i$ where $t_i = 2r_{\parallel}/U_{\text{laser}}$ denotes the interaction time, or time of irradiation of the weld

Table 1
Beam profile parameters for the different cases.

Profile	C1	C2	C3
Symbol			
r_{\parallel} [mm]	0.65	2.50	0.65
r_{\perp} [mm]	2.50	0.65	0.65
P_d [kW/cm ²]	19.60	19.60	75.30

Table 2

Welding travel speed and derived parameters for the beam profiles C1 to C3.

	U_{laser} [mm/s]					Profile
	5.0	7.5	10.0	12.5	17.5	
t_i [s]	0.26	0.17	0.13	0.10	0.07	C1, C3
	1.00	0.67	0.50	0.40	0.29	C2
E_d [kJ/cm ²]	5.10	3.40	2.50	2.00	–	C1
	19.60	13.10	9.80	7.80	5.60	C2, C3

centreline. The energy density and interaction time related to each combination of beam profile and welding travel speed computed in this study can be found in [Table 2](#).

3. Model description

Melt pool physics in an alloy heated by a moving high-power laser beam can involve several phenomena described in the review by Sveinungsson et al. [13] and the references therein. In this study the laser power density is low enough to be in conduction welding mode. Cho et al. [14] gave evidence that in such circumstances liquid metal vaporisation is negligible. Kim and Kim [16] did show that multiple-Fresnel reflection is also negligible due to the low deformation of the free surface. On the other hand, Saldi [17] observed that modelling of the free surface deformation is however important since it amplifies the heat transfer by thermocapillary convection and significantly contributes to the bead geometry. Ebrahimi et al. [18] observed that turbulence modelling has a negligible influence on melt flow when free surface deformation is taken into consideration. Bhatti et al. [19] did show that the temperature dependence of material properties has a significant effect on the temperature field (and on derived mechanical properties). Furthermore, the thermodynamic and transport properties of Ti–6Al–4V such as specific heat capacity and thermal conductivity undergo large variations with temperature when fusion occurs. The main characteristics of the thermo-fluid model of this study are thus to neglect turbulence, vaporisation and multiple-Fresnel reflections, to track the deformation of the liquid metal free surface and to include temperature dependent thermodynamic and transport properties.

3.1. Governing equations

A one-fluid approach for three dimensional and unsteady problem is followed to model the metal in both solid and liquid state with melting and re-solidification, and the gaseous shielding environment. The fluids are treated as immiscible, mechanically incompressible, and Newtonian. The small variations of the metal density with temperature compared to the metal density at the melting point are included through the Boussinesq approximation. To track the free surface deformation, an algebraic variant of the Volume Of Fluid (VOF) model originally developed by Hirt and Nichols [20] is applied. This variant was proposed by Ubbink [21] to sharpen the interface capturing when advecting the volume fraction of liquid metal, α . The system of equations thus governs the volume fraction, and the conservation of mass, momentum, and internal energy. Expressed as implemented, it writes

$$\frac{\partial \alpha}{\partial t} + \nabla \cdot (\alpha \vec{U}) + C_\alpha \nabla \cdot [\alpha(1-\alpha)\vec{U}_c] = 0 \quad (2)$$

$$\frac{\partial \rho}{\partial t} + \nabla \cdot (\rho \vec{U}) = 0 \quad (3)$$

$$\begin{aligned} & \frac{\partial(\rho \vec{U})}{\partial t} + \nabla \cdot (\rho \vec{U} \vec{U}) \\ & - \nabla \cdot \left[\mu \left(\nabla \vec{U} + (\nabla \vec{U})^T \right) - \frac{2}{3} \mu (\nabla \cdot \vec{U}) \mathbf{I} \right] \\ & = -\nabla p + \rho_m [1 - \beta(T - T_m)] \vec{g} + \vec{F}_s + \vec{S}_D \end{aligned} \quad (4)$$

$$\begin{aligned} & \frac{\partial(\rho c_p T)}{\partial t} + \nabla \cdot (\rho c_p T \vec{U}) \\ & = \nabla \cdot (k \nabla T) - \rho_1 h_{st} \left[\frac{\partial(\alpha f_i)}{\partial t} + \nabla \cdot (\alpha f_i \vec{U}) \right] + \dot{Q}_{\text{laser}} \end{aligned} \quad (5)$$

where t is the time, ρ the one-fluid density, \vec{U} the velocity vector, p the gauge pressure, and T the temperature. \mathbf{I} denotes the identity matrix. The one-fluid density, dynamic viscosity, μ , specific heat capacity at constant pressure, c_p , and thermal conductivity, k , are defined in the next section.

In equation (2), the third term is the free-surface sharpening term, which is only effective at the interface due to the factor $\alpha(1-\alpha)$. The numerical compression velocity, \vec{U}_c , is defined as a function of the relative flux at the cell faces [21]. In this study, the numerical compression factor is set to $C_\alpha = 1$ to satisfy conservation.

In the momentum conservation equation the second term in the right hand side is the body force due to the gravitational acceleration, \vec{g} , and the buoyancy in the liquid alloy. β is the volume expansion coefficient, ρ_m the working material density at the melting temperature $T_m = 0.5(T_s + T_l)$, where T_s and T_l are the solidus and liquidus temperatures, respectively. The next term, \vec{F}_s , is the surface force arising from the surface tension. It is treated as a volumetric force, $\vec{F}_s = (\vec{f}_{s,n} + \vec{f}_{s,\tau})|\nabla\alpha|$, as introduced by Brackbill et al. [22]. The first component along the local direction normal to the free surface, $\vec{f}_{s,n} = \sigma\kappa\vec{n}$, is the capillary force, and the normal component, $\vec{f}_{s,\tau} = \nabla_\tau\sigma$, is the thermocapillary force. Additional treatment is needed in the presence of two fluid phases with densities differing by several orders of magnitude, as in this study. It consists in using the multiplier introduced by Brackbill et al. [22], so that fluid acceleration by the surface tension force remains independent of the fluid density. Therefore, the volumetric surface force is written as

$$\vec{F}_s = \left[\sigma\kappa\vec{n} + \frac{d\sigma}{dT}(\nabla T - \vec{n}(\vec{n} \cdot \nabla T)) \right] |\nabla\alpha| \frac{2\rho}{\rho_1 + \rho_2} \quad (6)$$

The last factor in Eq. (6) is the multiplier. ρ_1 denotes the metal alloy density, and ρ_2 the gas atmosphere density. The unit vector locally normal to the free surface and the interface curvature are respectively defined as

$$\vec{n} = \frac{\nabla\alpha}{|\nabla\alpha|} \quad (7)$$

$$\kappa = -\nabla \cdot \vec{n} \quad (8)$$

The last term of Eq. (4) is the Darcy momentum sink term acting in the solid/liquid metal transition region (or mushy zone) to force the fluid velocity to zero in the solid region. This damping term is modelled by analogy with porous media using the isotropic Blake-Kozeny model described by Singh et al. [23]. It writes

$$\vec{S}_D = -C_D \frac{(1-f_i)^2}{f_i^3 + \varepsilon_D} \vec{U} \quad (9)$$

where C_D is a large constant ($=10^6$) that is inversely proportional to the permeability of the porous media, whereas ε_D is a small constant ($=10^{-3}$) to avoid division by zero in the solid phase. The liquid fraction, f_i , is described by an increasing function of temperature varying from zero in the solid state ($T \leq T_s$) to one in the liquid state ($T \geq T_l$) since metal alloy phase change is non-isothermal. In this study, the continuous function with continuous derivative proposed by Rösler and Brüggemann [24] is applied. It is given by

$$f_i = \frac{1}{2} \left[\operatorname{erf} \left(\frac{4(T - T_m)}{T_l - T_s} \right) + 1 \right] \quad (10)$$

In the internal energy conservation equation viscous dissipation is neglected because the Prandtl number as well as the velocity magnitude within the melt pool are low. The second term in the right hand side is related to metal melting and re-solidification. It includes the convection of latent heat that occurs in the fusion of alloys. This effect, which tends to widen the melt pool, is often neglected. h_{sf} is the latent heat of fusion. The last term of Eq. (5), \dot{Q}_{laser} , is the rate of heat input due to the laser beam. It is modelled through a volumetric source term that is only effective at the interface, according to

$$\dot{Q}_{laser} = \dot{q}_{laser} |\nabla \alpha| \frac{2\rho}{\rho_1 + \rho_2} \quad (11)$$

where \dot{q}_{laser} is the laser power density distribution defined in Eq. (1). The last factor in the right-hand side is the same multiplier as in Eq. (6).

3.2. Material properties

The one-fluid thermodynamic and transport properties are defined according to the following mixture model:

$$\rho = \alpha \rho_1 + (1 - \alpha) \rho_2 \quad (12)$$

$$\mu = \alpha f_l \mu_1 + (1 - \alpha) \mu_2 \quad (13)$$

$$c_p = \alpha [f_l c_{p,1,l} + (1 - f_l) c_{p,1,s}] + (1 - \alpha) c_{p,2} \quad (14)$$

$$k = \alpha [f_l k_{1,l} + (1 - f_l) k_{1,s}] + (1 - \alpha) k_2 \quad (15)$$

where the indices 1 and 2 stand for the primary (Ti-6Al-4V) and the secondary (argon gas) material, respectively. The subscript l denotes the liquid state and s the solid state. Due to the Boussinesq approximation, $\rho_1 = \rho_{1,s} = \rho_{1,l}$. The thermodynamic and transport properties of the Titanium alloy Ti-6Al-4V are well documented in the solid state and the low temperature range of the liquid state. These data are presented in Table 3. Boivineau et al. [25] provided the solidus and liquidus temperatures. Mills [15] reported experimental measurements for the density, latent heat of fusion, viscosity, specific heat capacity and thermal conductivity. For convenience, curve-fitted expressions of these experimental data are used here. In this study the alloy and the shielding atmosphere contain negligible amount and no surface-active element, respectively. When defining the surface tension in Table 3 the coefficients σ_0 and $\frac{d\sigma}{dT}$ are thus constant. These coefficients, provided by Rai et al. [26], are set to $\sigma_0 = 1.6$ N/m and $\frac{d\sigma}{dT} = -2.6 \times 10^{-4}$ N/(m.K). The radiative emissivity is taken from Ref. [27], and the absorption

Table 3
Material properties of solid and liquid Ti-6Al-4V.

Parameter	Value	Validity range in K	Dimension
T_s	1873	–	K
T_l	1923	–	K
T_m	1898	–	K
ρ_1, ρ_m	4420.0	–	kg/m ³
μ_1	0.0035	–	kg/(m.s)
$c_{p,1,s}$	$\begin{cases} 483.04 + 0.215 T \\ 412.7 + 0.1801 T \end{cases}$	$\begin{cases} 298 \leq T < 1268 \\ 1268 \leq T < T_m \end{cases}$	J/(kg.K)
$c_{p,1,l}$	830.0	$T_m \leq T < 3000$	J/(kg.K)
$k_{1,s}$	$\begin{cases} 1.2595 + 0.0157 T \\ 3.5127 + 0.0127 T \end{cases}$	$\begin{cases} 298 \leq T < 1268 \\ 1268 \leq T < T_m \end{cases}$	W/(m.K)
$k_{1,l}$	$-12.752 + 0.024 T$	$T_m \leq T < 3000$	W/(m.K)
σ	$\sigma_0 + \frac{d\sigma}{dT}(T - T_m)$	$T_m \leq T < 3000$	N.m
h_{sf}	2.86×10^5	–	J/kg
β	8.0×10^{-6}	–	1/K
ε	$0.1536 + 1.8377 \times 10^{-4}(T - 298)$	$298 \leq T < 3000$	–
η	0.34	–	–

Table 4
Material properties of argon gas.

Parameter	Value	Dimension
ρ_2	1.6337	kg/m ³
μ_2	42.26×10^{-5}	kg/(m.s)
$c_{p,2}$	520	J/(kg.K)
k_2	0.0177	W/(m.K)

coefficient from Ref. [28].

Çengel [29] reported the thermodynamic and transport properties of argon gas. In the temperature range of this study, the specific heat capacity of this rare gas is almost constant. The temperature dependence of density, thermal conductivity and viscosity is neglected. The properties of the shielding gas are thus constants set at 300 K and reported in Table 4.

3.3. Computational domain, boundary, and initial conditions

Fig. 1 shows the computational domain. It is a rectangular cuboid which spans $40 \times 12 \times 4$ mm in $x, y,$ and z directions, respectively. Due to the symmetry of the geometry and process with respect to the xz plane, only half of the domain is simulated. The upper half (in z direction) is filled with argon gas, and the 2 mm-thick plate (Ti-6Al-4V workpiece) is located at the bottom of the domain. The initial solid-gas interface is depicted by a surface perpendicular to the z axis. The initial position of the laser spot is also illustrated with a red dot at $x = 10$ mm.

Fig. 2 shows the boundary conditions used for the numerical simulations at the end surfaces in the y and z directions. The gradients of all variables were set to zero at the two end surfaces in the x direction. At the Ti-6Al-4V/atmosphere interface, the radiation heat flux was also implemented as:

$$\dot{q}_{rad} = \varepsilon \sigma_B (T^4 - T_{amb}^4) \quad (16)$$

where $\sigma_B = 5.67 \times 10^{-8}$ W/(m².K⁴) is the Stefan Boltzmann constant, ε the emissivity (see Table 3), and $T_{amb} = 300$ K the ambient temperature. At the initial state, $t = 0$ s, the temperature field was set to T_{amb} , and the velocity and gauge pressure fields to zero. The natural convection heat transfer coefficient on the bottom and two end surfaces (in the x direction) of the workpiece was set to 20 W/(m².K). Furthermore, the volume fraction at the bottom half of the domain filled with the workpiece was initialized to $\alpha = 1$, and the upper half filled with the argon gas was initialized to $\alpha = 0$.

The computational domain is split into six regions with different grid resolutions (see Fig. 1). Three different grid sizes with 5 (grid 1), 10 (grid 2), and 15 (grid 3) hexahedral cells per millimetre in the melt pool region were examined. The variations between the results for grid 2 and grid 3 are much lower compared to the results for grid 1. The maximum deviation between the computed results (e.g. pool dimensions, temperature, and velocity fields) for grid number 2 and 3 is less than 5 %. Grid number 2 is thus used for the computations presented hereafter.

3.4. Solution method

The implementation is done in OpenFOAM®. This software, conceived by Weller et al. [30], is a field operation and manipulation class library distributed with a number of solvers for different continuum mechanical problems. Due to the availability of the source code, its libraries can be used to implement new solvers for other applications. The set of governing equations and the temperature dependent material properties described in sections 3.1-3.2 were implemented based on the original built-in solver interFoam. InterFoam is a finite volume solver capable of capturing the free surface of two incompressible fluids using a VOF method for isothermal flow with constant capillary force and constant material properties. The new features implemented can be seen

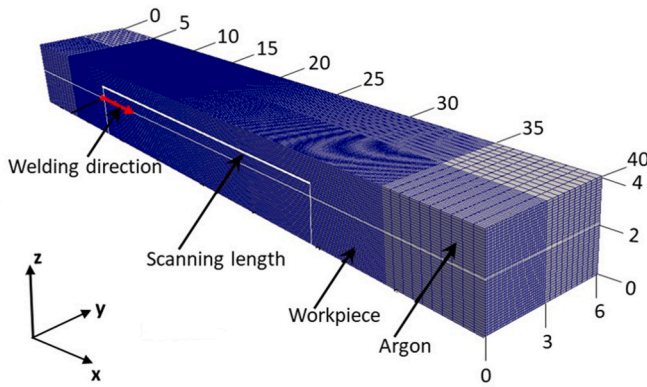


Fig. 1. Schematic of the computational domain, with dimensions in mm.

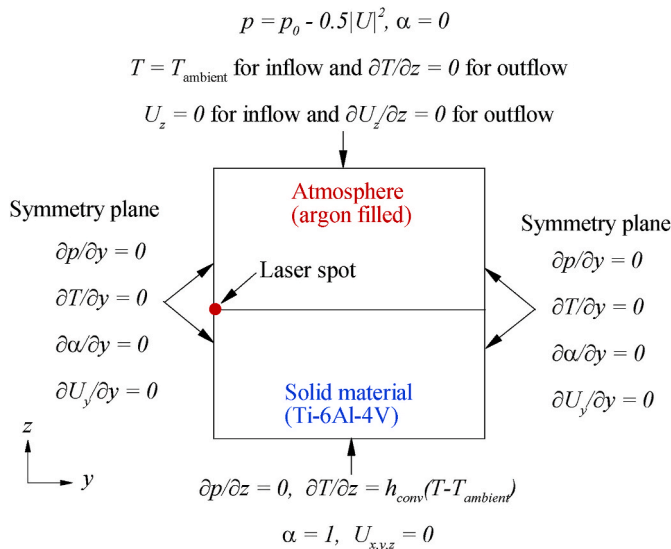


Fig. 2. Boundary conditions for the simulations.

in Eqs. (1)–(15) and are not repeated here. Consistently with the capillary force, the thermocapillary force was implemented with the sharp surface force (SSF) model introduced by Shams et al. [31].

In the process of solving the governing equations (2)–(5) the pressure-velocity coupling was computed using a Pressure-Implicit with Splitting of Operators (PISO) algorithm. For the convection term in the VOF-equation (2) Gauss van Leer scheme was used, which strictly bounds the volume fraction value between zero and one. For handling the convective terms of Eqs. (3)–(5) Gauss linear scheme that is a second order method was applied. Diffusive fluxes were discretized by central differencing scheme. The volume fraction transport equation was solved by MULES (Multidimensional Universal Limiter with Explicit Solution) algorithm to guarantee boundedness of its solution. The highly coupled set of equations (2)–(5) was solved applying an adjustable time stepping with a maximum CFL number set to 0.2, and a maximum allowed time step size of 10^{-5} s. The convergence criteria imposed on the (final) residuals at each physical time step when solving for α , p , \vec{U} and T was 10^{-12} , 10^{-8} , 10^{-8} , and 10^{-10} , respectively. Each task was executed in parallel on six cores (Intel® Xeon(R) Gold 6244 CPU @ 3.60 GHz \times 16) of a computing cluster. These computations were performed without Adaptive Mesh Refinement (AMR). The simulation time per task took about 21 days and several separate simulations were performed at the same time. It is also worth mentioning that a refinement criteria based on the α -field was developed afterwards to apply structured AMR. Using AMR reduces the time necessary for processing a task down to about four

days.

4. Experimental procedure for solver verification

The experiments were carried out in a high-power laser processing cell of University West with controlled atmosphere and a motion-controlled laser beam welding equipment. This equipment consists of a water-cooled high-power ytterbium-doped fibre laser, a CNC gantry fixture, and a camera vision system mounted in a welding chamber. The chamber was built to provide a consistent argon environment during welding. The oxygen level of the chamber, measured by a gas analyser from WITT Germany (Oxybaby 6i O₂/CO₂), was below 0.1%. In this chamber, a CNC gantry from Isel® Germany (mod. M40) was used to manipulate the welding tool from Permanova Lasersystem AB. The laser beam was generated by a 6 kW IPG Ytterbium fibre laser system (mod. YRL-6000-S) with a 1070 nm wavelength. It was guided through an 800 μ m core diameter optical fibre to the welding tool. The welding tool comprised a 160 mm focal length collimator and a 300 mm focal length focusing lens. It was mounted at an angle of 5° with respect to the normal direction of the workpiece surface to avoid the back reflections of the laser beam. The focused beam was characterized by a Rayleigh length of 12.2 mm and a spot size diameter in the focal plane of 1.5 mm. The laser power was continuous wave (CW) and the laser beam was consistently focused on the surface of the workpiece to perform the conduction welding. The dimensions of the Ti-6Al-4V plates were 300 mm \times 40 mm and 3.2 mm in thickness. The plates were cleaned with acetone prior to welding. In the experiments the measured beam intensity profile was almost uniform, thus a top-hat power density distribution was implemented in the computational software to perform the solver verification. Three welding cases were conducted with the same 1 kW continuous wave laser power and welding travel speeds of 5 mm/s, 7.5 mm/s and 10 mm/s. Each condition was repeated three times producing similar 50 mm long seam welds. After re-solidification, the samples were scanned with a light interferometry profilometer from Filmetrics with a resolution of 0.92 μ m to measure the shape of the bead surface. The depression left at the laser stop location was also documented. The samples were cross sectioned at the half-length of each weld, polished and etched with 8% fluoroboric acid solution prior to macroscopic investigation.

5. Results and discussion

5.1. Solver verification

The experimental test cases described in Section 4 were simulated to verify the solver's reliability. Further information about the heat input modelling can be found in Ref. [32]. The computations were run up to the time $t = 2$ s to obtain a fully developed melt pool in all three investigated welding conditions. Similar development time was also observed in the experiments. The laser heat source was then switched off and the computations continued to simulate also the solidification step.

The first element verified is the geometry of the lower part of the bead, which can be accessed through the computed isotherms when the melt pool is fully developed. Fig. 3 thus visualizes on the left hand side the micrograph images showing the experimental post-solidification fusion zone (FZ) and heat affected zone (HAZ). For comparison, in the right hand side, the numerically predicted isotherms are plotted at time $t = 2$ s in the plane $x = 20$ mm for $U_{\text{laser}} = 5$ and 10 mm/s. The plots marked T_{solidus} and T_{liquidus} visualize the T_s and T_l isotherms, respectively. The $T_{\alpha \rightarrow \beta}$ plot stands for the $\alpha \rightarrow \beta$ transition isotherm that is at 1268 K [15]. The results for the temperature profiles demarcating the mushy zone are in very good agreement with the curved edge of the FZ delimiting the workpiece area with very large grain size. The HAZ coincides with smaller grains and might extend over a temperature range of about 600–900 K below the solidus temperature depending on the

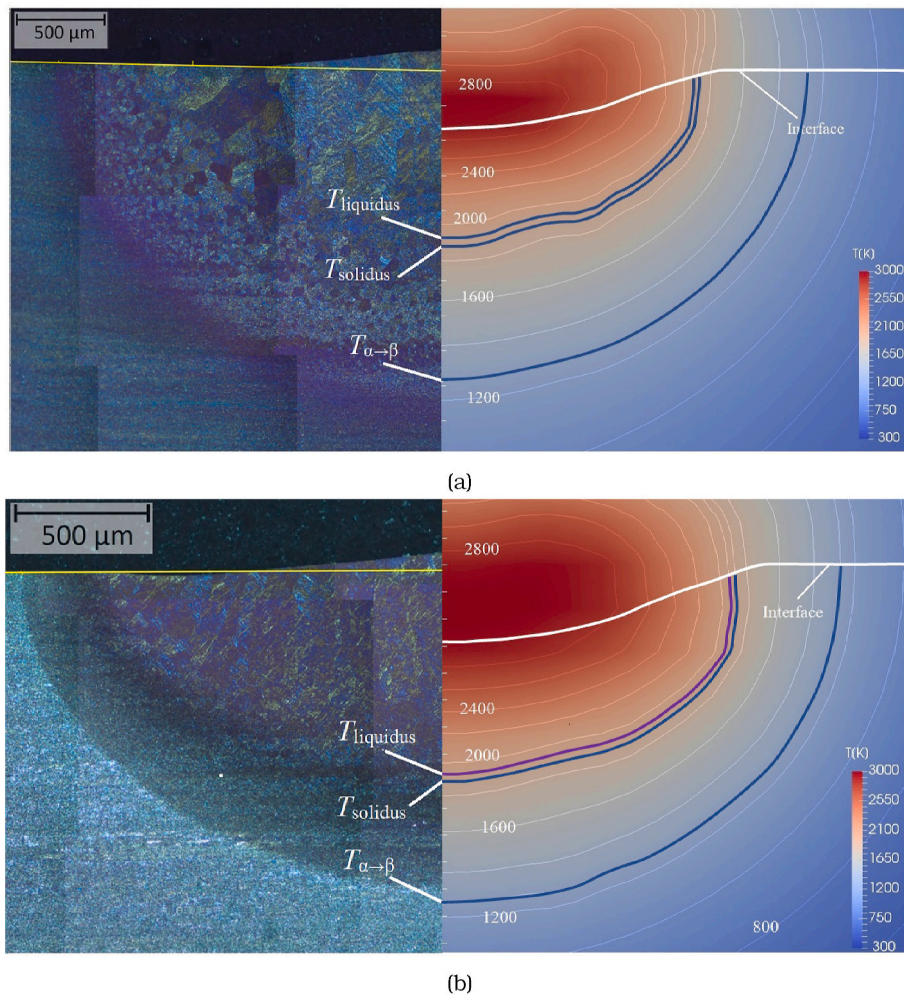


Fig. 3. Comparison between the metallographic image of the post-solidification melt pool shape (left) and the predicted melt pool isotherms (right) in a cross section at $t = 2.0$ s; (a) $U_{laser} = 5$ mm/s, (b) $U_{laser} = 10$ mm/s. The isotherm lines vary from 800 K to 2800 K with an increment of 200 K.

welding conditions, in particular the cooling rates. The comparison is thus more difficult concerning the outer part of that region. Anyway, the $\alpha \rightarrow \beta$ transition temperature provides a useful indication; its computed isotherm is also in good qualitative agreement with the outer edge of the HAZ observed in the experimental cross-cuts. Table 5 presents a quantitative comparison between the computed and the experimental weld penetration depth at the different welding travel speeds. The experimental measurements accuracy is ± 0.1 mm due to the uncertainty when locating the border between FZ and HAZ. The results show that the penetration is predicted accurately compared to the experimental data.

The predicted geometry of the bead top surface cannot be verified with Fig. 3 as the curvature of the melt pool free surface changes upon solidification. Fig. 4 compares the computed and measured shape of the top border of the solidified bead for two different laser travel speeds. The experimental measurement uncertainty is 0.01 mm. It can be seen that the numerical model can well predict the experimental shape after solidification, especially when it comes to the maximum value reached at

Table 5
Comparison between computed (D_{comp}) and experimental (D_{exp}) weld penetration depth, and their deviation (δ_D) at different welding travel speeds.

U_{laser} [mm/s]	D_{comp} [mm]	D_{exp} [mm]	δ_D (%)
5	0.96	1.0 ± 0.1	4.0
7.5	0.87	0.9 ± 0.1	5.2
10	0.79	0.8 ± 0.1	1.2

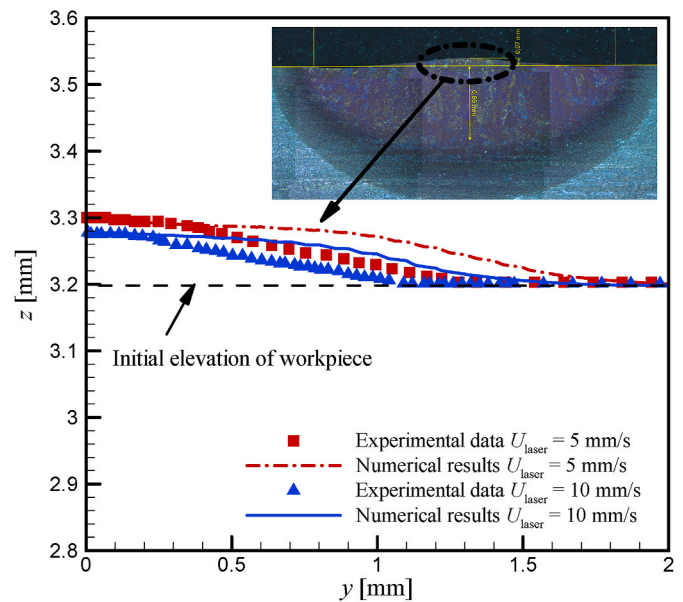


Fig. 4. Comparison in a cross-section between the numerical results and the experimental measurements of the shape of the weld top surface after solidification.

the centre of the bead. The small deviations at the edge of the bead in the simulated results compared to the experimental measurements might be attributed to the physical laser power distribution. When this last one was measured, small deviations from the top-hat used in the simulations were indeed observed at the edge of the laser spot.

The last verification includes the geometry of the depression (or crater) left at laser switch off. Fig. 5 shows the top-view of a workpiece after solidification for $U_{\text{laser}} = 5$ and 10 mm/s. It can be observed that the model predicts well the width of the bead and the crater's contour.

5.2. Melt pool geometry for the beam shapes C1 to C3 - results

The test cases C1, C2 and C3 described in Section 2 for non-uniform beam profiles with Gaussian-elliptic and Gaussian distribution are now addressed. The results confirming former knowledge are indicated when presented while other results are discussed in section 5.4 in the light of all the computed fields.

The numerical simulations aimed at obtaining a fully developed melt pool. It was observed that the α -field was controlling the time needed to reach quasi-steady state in the laser beam reference frame, while the velocity and temperature fields used to stabilize faster. As the α -field is bounded, its development was examined through the melt pool volume $\sum_i (af_i \Omega_i)$ where Ω_i denotes the volume of cell i . The evolution of this volume during time is reported in Fig. 6 for the beam profile C1 and travel speeds ranging from 5 to 10 mm/s. It can be seen that the pool development time increases when the welding travel speed is decreased. When considering the full set of test cases, it was observed that the melt pool volume does not change noticeably after at most $t = 1.5$ s when the welding travel speed is $U_{\text{laser}} \geq 7.5$ mm/s, and $t = 3.8$ s when $U_{\text{laser}} = 5$ mm/s. The results presented hereafter are thus computed until time $t = 2.0$ s when $U_{\text{laser}} \geq 7.5$ mm/s and until time $t = 4.0$ s when $U_{\text{laser}} = 5$ mm/s.

Fig. 7 visualizes the computed melt pool geometry for the different laser spot profiles at $U_{\text{laser}} = 5$ mm/s. The plots represent sections of the melt isosurface $af_i = 0.5$ that are perpendicular to the welding travel direction and pass through the laser beam centre. It can be seen that the deformation of the free surface, with maximum depression at the pool center in $y = 0$ mm, is more pronounced for the beam profile C3 (Gaussian profile) than for the two other cases. The laser energy delivered to the simulated workpiece is the same (at fixed U_{laser}) for the three beam profiles as P_{laser} and η are kept unchanged. But the elevated peak intensity of the power density distribution C3 (see Table 2) is expected to sharpen the temperature gradients, as confirmed later on. This in turn enhances the thermocapillary convection and free surface deformation. Accordingly, the computational results show that the deformation of the free surface gradually weakens when the welding travel speed is

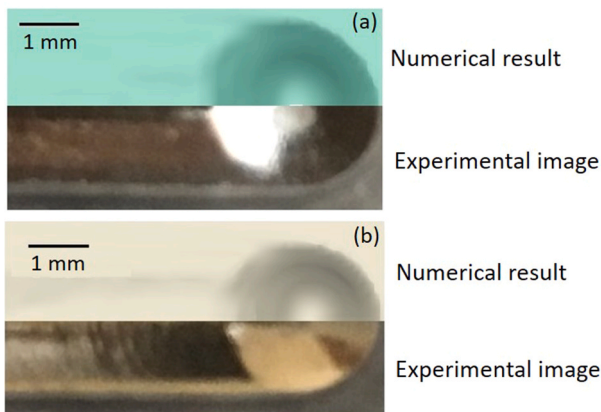


Fig. 5. Top view of a workpiece after solidification; (a) $U_{\text{laser}} = 5$ mm/s, (b) $U_{\text{laser}} = 10$ mm/s.

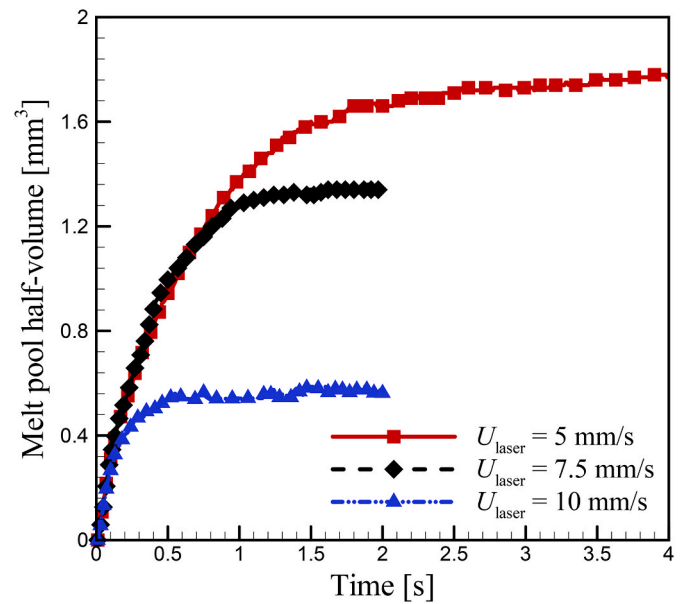


Fig. 6. Melt pool volume as a function of time; beam profile C1.

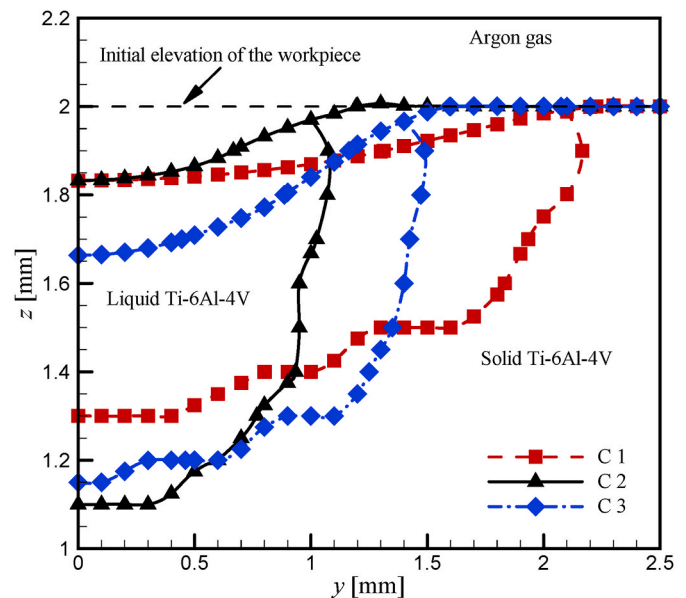


Fig. 7. Effect of the beam profiles on the pool geometry in the cross section at the beam centre; $U_{\text{laser}} = 5$ mm/s and $t = 4.0$ s.

increased.

Fig. 8 shows the melt pool half-width as a function of the welding travel speed for the three beam profiles. It is observed, as reported in earlier studies, that for each beam profile the pool width decreases when the welding travel speed is increased, that is when the interaction time is decreased (see t_i in Table 2). Also, the melt pool is always the widest for case C1 (transverse Gaussian-elliptic), as seen in Figs. 7 and 8. Ayoola et al. [10] did a similar finding in their experimental investigation using elliptical spots with smaller aspect ratio than in this study. The fully developed pool width computed with the longitudinal Gaussian-elliptic profile C2 and the Gaussian profile C3 are now compared. These profiles are characterized by the same transverse radii and the same energy density at given welding travel speed (see r_{\perp} and E_d in Tables 1 and 2). Figs. 7 and 8 show that at all the welding travel speeds computed the pool is significantly wider with C3 than with C2. This observation thus

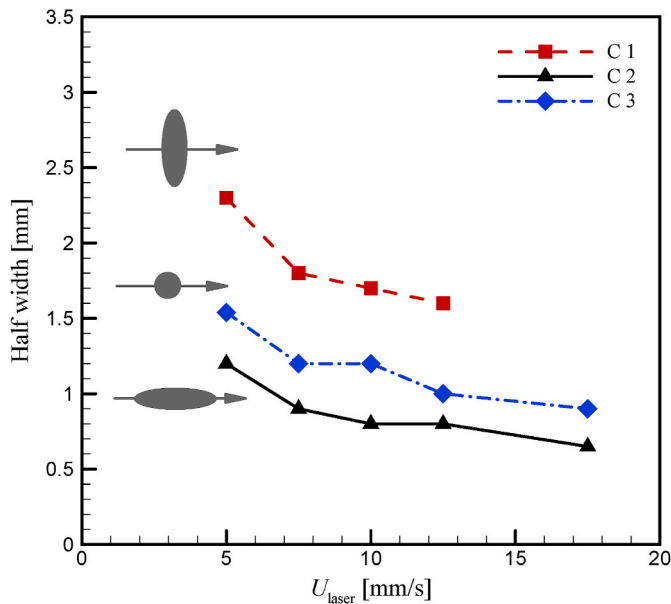


Fig. 8. Melt pool half-width as a function of the welding travel speed for each of the three beam profiles.

differs from the result of Ayoola et al. [10] who did not notice any significant change in pool width when performing similar comparisons with smaller beam elongation, that is lower power density variation between the profiles. Possible reasons for these differences are discussed in section 5.4.

The melt pool side views plotted in Fig. 9 for $U_{laser} = 5 \text{ mm/s}$ show that the deepest part of a pool can be located after the beam spot centre has passed. The pool penetration depths gathered in Fig. 10 for the different beam profiles and welding travel speeds are thus extracted from melt pool side views. As reported in previous experimental studies e.g. Refs. [2,33], it can be checked in Fig. 10 that for each beam profile the penetration depth decreases when the welding travel speed increases due to the decrease in interaction time and energy density; see t_i and E_d in Table 2. Furthermore, it can be seen in Figs. 9 and 10 that the penetration depth reached with the transverse Gaussian-elliptic beam

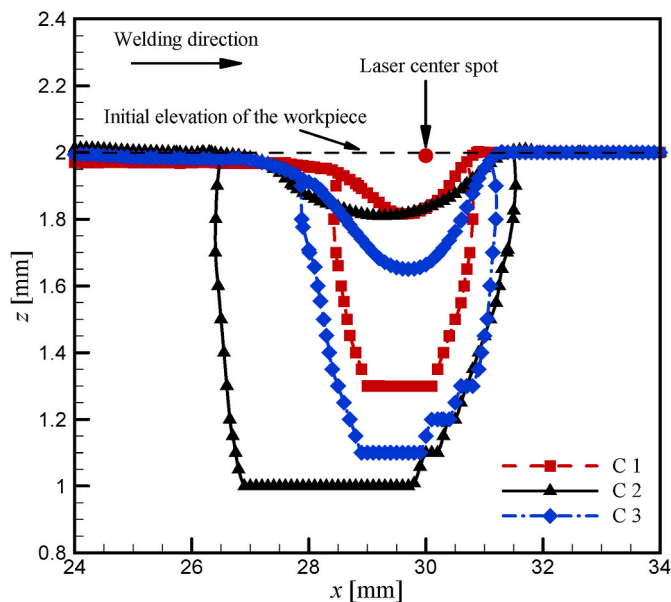


Fig. 9. Effect of the beam profiles on the pool geometry in the symmetry plane; $U_{laser} = 5 \text{ mm/s}$ and $t = 4.0 \text{ s}$.

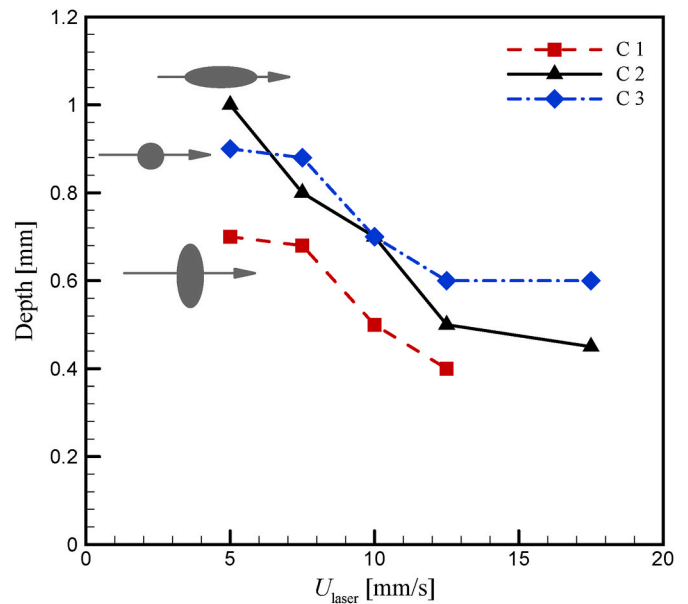


Fig. 10. Melt pool penetration depth as a function of the welding travel speed for each of the three beam profiles.

profile C1 is always very shallow compared to the other profiles. Similar observations were made in the experimental study of Ayoola et al. [10]. This result can be explained by the low integrated power density (Table 1) combined with the low interaction time for C1 that result in a lower range of energy density compared to C2 and C3. Besides, the Gaussian profile C3, which is associated with the highest and sharpest laser power density distribution, results accordingly in the deepest pool penetration. However, this is only observed at welding travel speeds $U_{laser} \geq 7.5 \text{ mm/s}$. At the lower welding travel speed $U_{laser} = 5 \text{ mm/s}$ a different situation can be seen in Figs. 9 and 10. The melt penetration depth is then clearly the highest with the beam profile C2 rather than with C3. It suggests that other factors than the sharpness of the beam power density distribution might enter into play.

Results that are difficult to access through experimental observation are from now examined. The effect of the three beam profiles on the melt

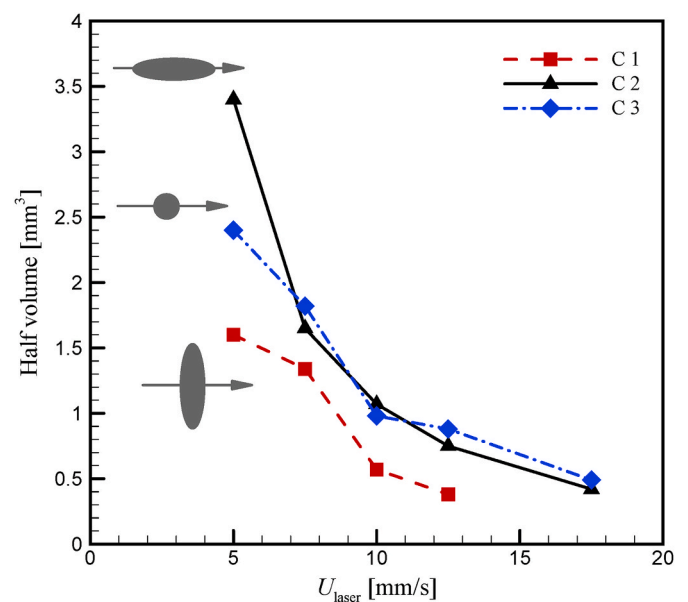


Fig. 11. Melt pool half-volume as a function of the welding travel speed for each of the three beam profiles.

pool volume is visualized at the quasi-steady state in Fig. 11. As expected, for each beam profile the volume of fused alloy decreases when increasing the welding travel speed since the interaction time and energy density are then decreased. Besides, it can be seen that the transverse and the longitudinal Gaussian-elliptic beam profiles C1 and C2 do not lead to the same pool volume when operated at the same welding travel speed. Therefore, the conjecture made by Ayoola et al. [10], inferring from the principle of energy conservation that the melt pool volumes had to be kept unchanged when changing the orientation of the elliptic spot, is not confirmed by the present study. This result is discussed in section 5.4. Furthermore, it can clearly be seen in Fig. 11 that at the welding travel speeds $U_{\text{laser}} \geq 7.5$ mm/s the laser beam profiles C2 and C3 lead to very similar volumes of melted metal. The lower pool width and depth (Figs. 8 and 10) of case C2 is counterbalanced by a higher pool length (Figs. 9 and 13). At the lower travel speed $U_{\text{laser}} = 5$ mm/s, the fused volume is about 30 % larger with the longitudinal Gaussian-elliptic spot C2 than with the significantly sharper and more intense Gaussian spot C3. It supports that the link between beam power density distribution and melt pool volume is not straightforward, and cannot simply be inferred from heat conduction principles alone, as suggested by Sundqvist et al. [12].

5.3. Melt pool thermo-hydrodynamics for the beam shapes C1 to C3 - results

Fig. 12 visualizes top views of the melt isosurface $af_i = 0.5$ and the workpiece with isotherms plotted on these liquid and solid surfaces for the beam profiles C1 to C3 at the welding travel speed $U_{\text{laser}} = 5$ mm/s. The applied non-uniform laser power density distribution, \dot{q}_{laser} , is also reported on each melt pool. The three plots of Fig. 12 are at the same scale. When comparing similar plots from time 3.9–4 s every 0.01 s the isotherms remain the same (in the laser beam reference frame) except at the pool rear where some small fluctuations are observed. Considering the isotherms on the melt pools, it can be seen that the beam profile C3, with highest power density peak value, leads as expected to a significantly larger maximum temperature compared to C1 and C2. The case C3, with sharpest power density distribution, leads accordingly to the closest isotherms, in particular within the laser spot area. It is observed that with the beam profile C2 the maximum temperature at the pool surface is about 200 K higher than with C1 while these elliptical power density distributions differ only by their orientation. Considering now the isotherms in the re-solidified alloy behind the pool, the distance between consecutive isotherms is shorter with C2 than with C1 and C3. The thermal energy entering the heat affected zone is thus dissipated over a shorter distance from the pool edge with C2 as visualized by the

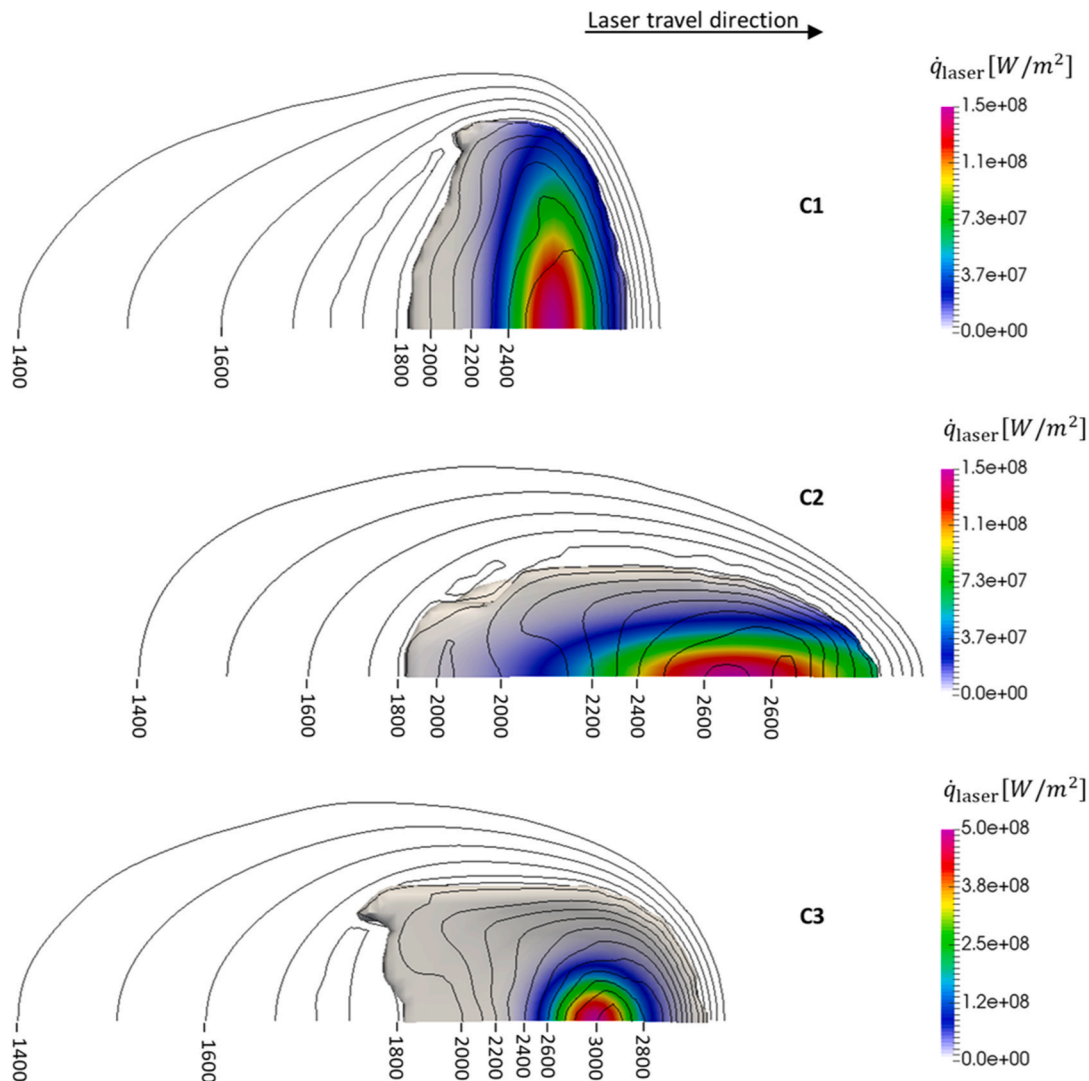


Fig. 12. Top view (z-plane) of the isotherms for the beam profiles C1, C2 and C3 at $U_{\text{laser}} = 5$ mm/s and $t = 4$ s. Isolines from 1400 to 3000 K with an increment of 100 K.

closer 1400 K - isotherm. However, the energy density E_d (see Table 2) is the same for the profiles C2 and C3, while E_d is significantly lower for C1.

Fig. 13 shows top views of the melt isosurface $af_1 = 0.5$ with velocity vectors plotted on that surface. The results are presented for the same conditions as in the previous figure. For each case it can be seen that the velocity vectors in the laser spot area (see Fig. 12) are oriented radially from the spot centre, due to the thermocapillary force that pushes the liquid metal outwards. Further away towards the pool lateral edge the fluid takes a counterclockwise path under the combined effect of the thermocapillary force and the welding travel speed. A counterclockwise vortex is also observed at the rear of the pool for each beam shape. This vortex might cause some instabilities in the flow and the small temperature fluctuations noticed earlier at the pool rear. Besides, as the power density distribution C1 is designed to lead to C2 by simple rotation of π rad about the beam axis, a similar rotation can be applied to the pool C1 for comparison with the pool of C2. Then, it can be seen that the thermocapillary flow, the high velocity magnitude at C1-pool shoulder, as well as the shape of the rear swirl are very similar. However, the melt flow at the pool free surface exhibit also specificities depending on the power density distributions. With C1 the vortex is located at the outer

edge; it is observed to move closer to the x -axis (or laser spot path) when the travel speed is increased. The vortex observed with C3 shrinks at the largest welding travel speed of this study. On the contrary, with C2 the rear vortex does not change noticeably in the range of welding travel speeds investigated. Another specificity is the maximum velocity reached by the fused alloy. Very few melt pool velocity measurements are available. Using in situ X-radiography and tracer particles Aucott et al. [34] measured instantaneous melt flow velocities in the different context of a welding arc heat source and a steel alloy with surfactant. The resultant average flow velocity was measured to be about 0.15 m/s and the largest maximum velocity, reached with the largest amount of surfactants, was 0.54 m/s. Anyhow, the melt pool velocities computed in the present study are of same order. It can be seen in Fig. 13 that for the beam profile C1 the maximum metal alloy velocity is reached at the outer and front part of the pool surface. It is perpendicular to the beam travel direction and clearly results from the thermocapillary acceleration, thus from the temperature gradient. With C2 the maximum velocity is along the pool centreline, in the rear vortex area. This does not coincide with the location of the maximum velocity for C1 after rotation by π rad about the beam axis. Moreover, it is directed along the beam travel speed, against the thermocapillary flow arising from the laser spot

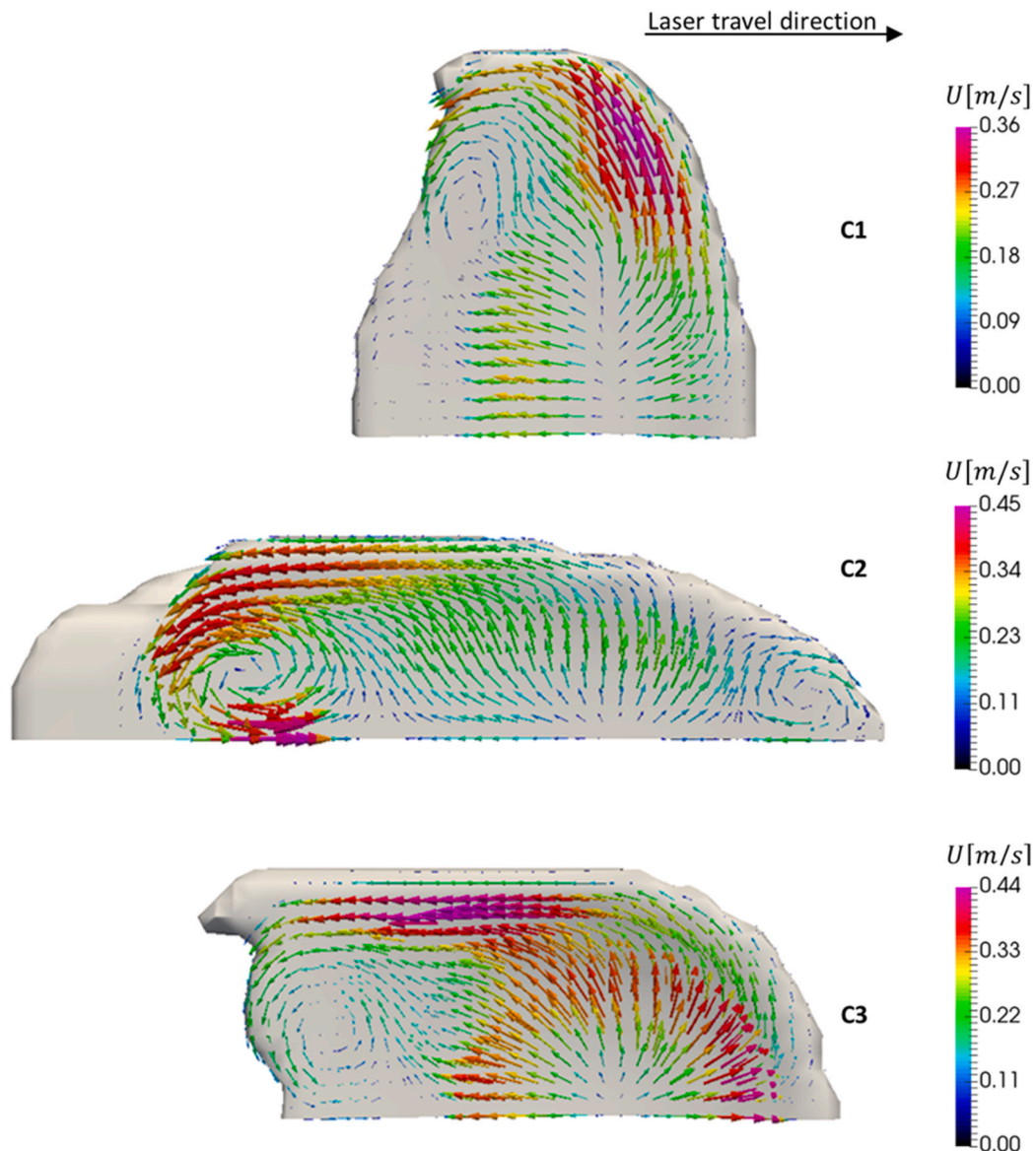


Fig. 13. Top view of the velocity vectors at the melt pool free surface for the beam profile C1, C2 and C3 at different welding travel speeds.

area, while its value is almost two orders of magnitude larger than the travel speed.

Fig. 13 (C2) shows also that the space left between the rear vortex and the pool outer edge is wider than the space between the vortex and the symmetry plane. As at standard pressure the liquid alloy is an incompressible fluid, the lower space left for forward flow needs to be compensated by an increased velocity to maintain the mass flow rate. Thus the location and direction of the maximum velocity for C2, as well as its larger value compared to the maximum velocity obtained with C1. For C3 the maximum velocity is observed along the lateral pool edge, and parallel to the laser beam travel direction. Its value of 0.44 m/s is almost two orders of magnitude larger than the welding travel speed,

implying that it is also governed by the thermocapillary acceleration. This maximum velocity is about 20% larger than for C1, which is consistent with the higher sharpness and intensity of the beam profile C3 compared to C1. However, the velocity magnitude is largest for C2, in spite of C2's weaker power density distribution compared to C3. Finally C2 shows one unique feature that is the presence of clockwise rotating flow in the front area of the pool. This rotating flow is not recirculating since it is not separated from the main stream, as will be seen in the sequel.

It was checked that in the pool bulk the fully developed fields are quasi-steady when observed in the laser beam reference frame. Streamlines can thus be used to investigate further the flow dynamics

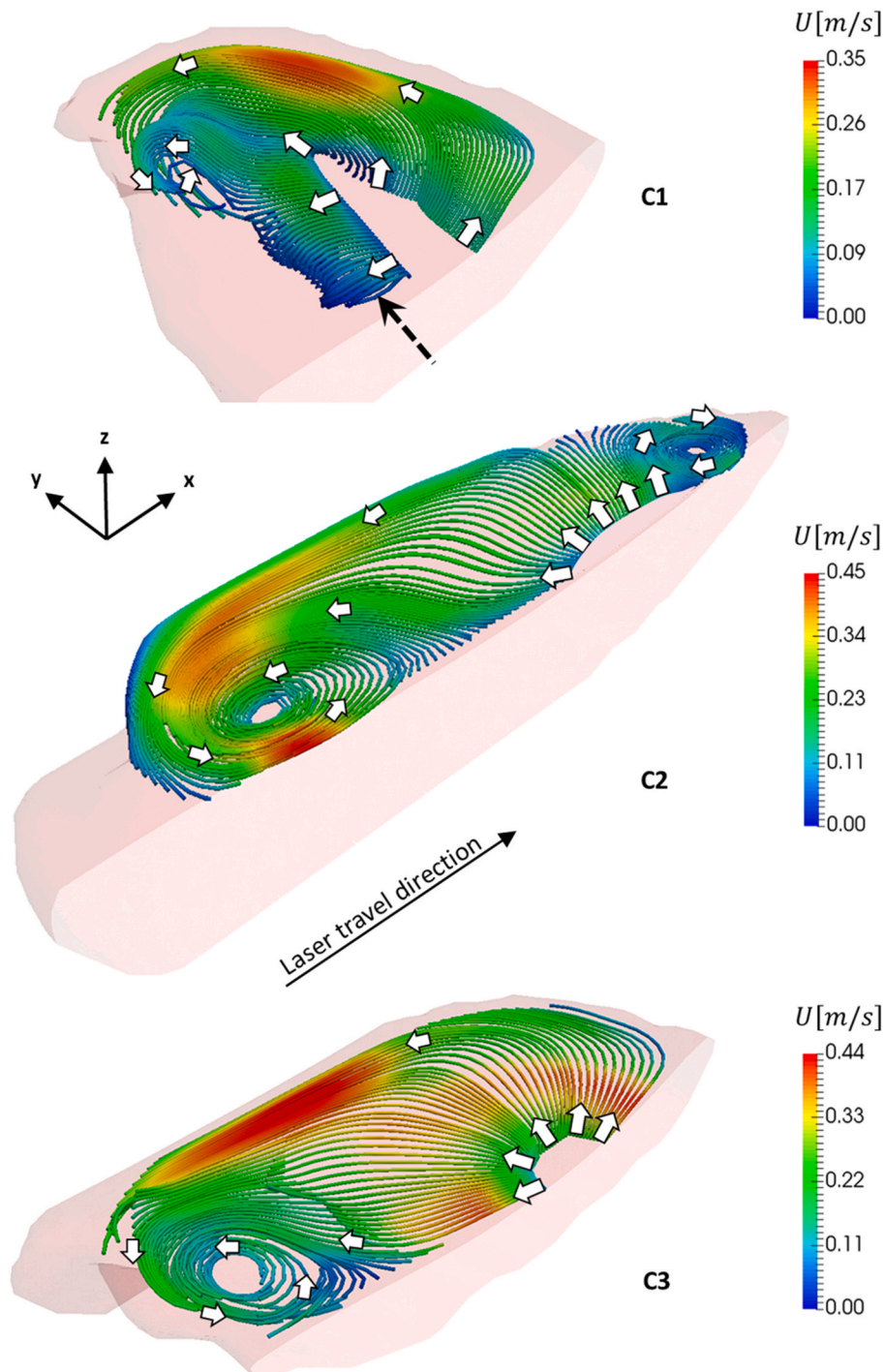


Fig. 14. Streamlines in the melt pool, close to the free surface, for the beam profile C1 to C3 and $U_{\text{laser}} = 5 \text{ mm/s}$, $t = 4 \text{ s}$.

deeper in the melt pool. Fig. 14 shows streamlines in the fused alloy, in a close vicinity of the free surface, for the beam profiles C1 to C3 at $U_{\text{laser}} = 5 \text{ mm/s}$. The streamlines are plotted from sets of line sources. The white arrows, that are larger in the beam spot area, indicate the flow direction. Combined with Figs. 12 and 14 (C1) shows that the fused metal pushed in the laser travel direction from the beam spot area is cooled while it successively flows along the melt pool front and side edges and continues towards the rear vortex. For the profiles C2 and C3 the streamlines from the beam spot area show a pattern similar to C1, although more stretched along the travel direction rather than the

transverse direction, or being more isotropic in accordance with the beam profile. The clear exception is the swirling structure at the front of C2, that is fed with hot fluid coming from the nearby beam spot area. It is characterised by a centripetal flow as all the swirling structures observed. Considering now the rear part of the pool, it can be seen that with C1 the heated fluid pushed out of the laser spot area against the travel direction does not reach the rear re-solidification front. Instead, it wraps about a horizontal axis oriented along the transverse direction and indicated in the figure with a dotted arrow. Also the swirling structure at the pool rear of C1 is significantly smaller and flows at lower

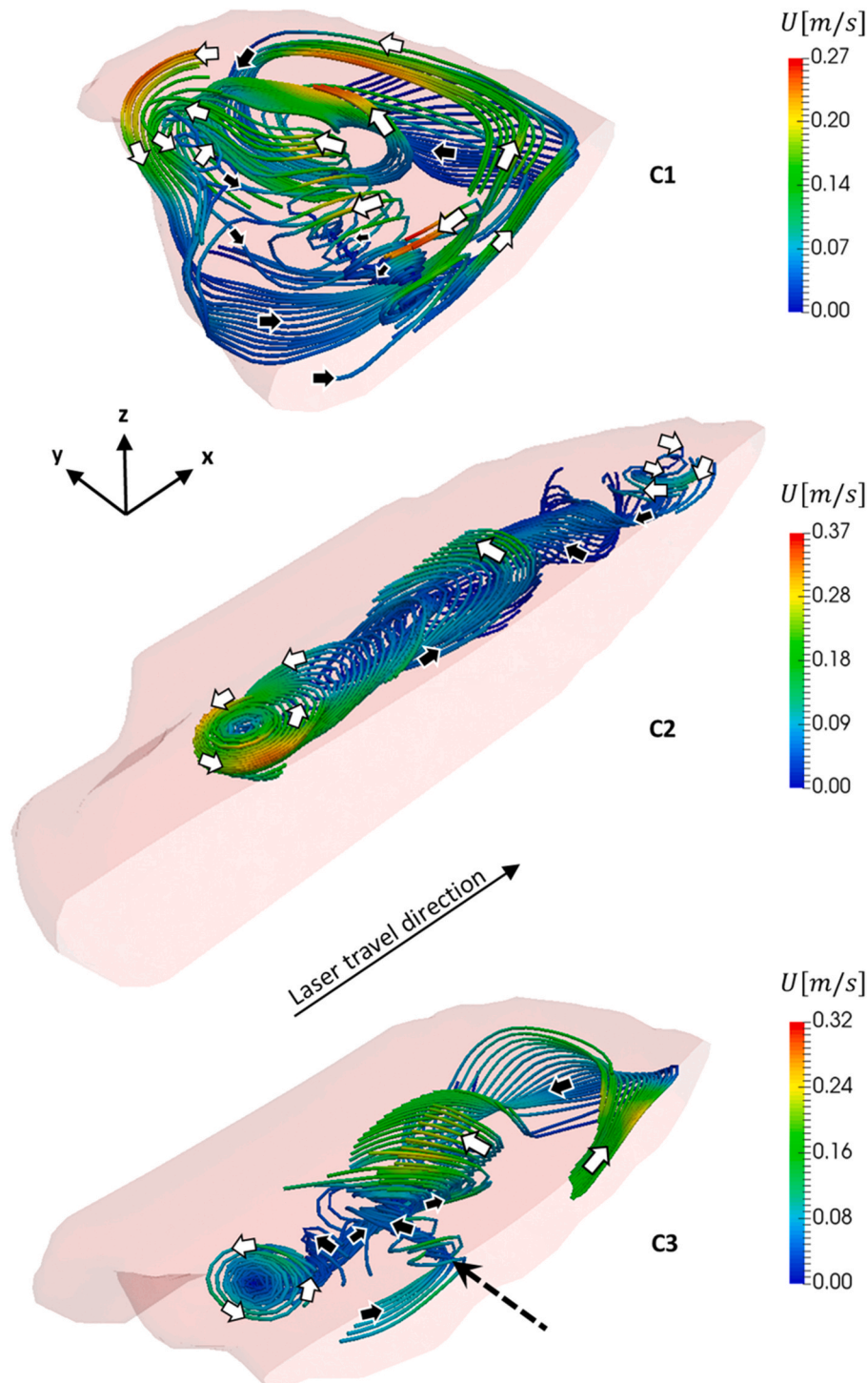


Fig. 15. Streamlines in the melt pool, at some distance below the free surface, for the beam profiles C1 to C3 and $U_{\text{laser}} = 5 \text{ mm/s}$, $t = 4 \text{ s}$.

velocity compared to C2 and C3.

Fig. 15 visualizes streamlines plotted deeper into the melt pool for the beam profiles C1 to C3 and the same laser travel speed as in the previous figure. Streamlines marked with black arrows are deeper into the pool than those marked with white arrows. With the help of Fig. 12 it can be seen that for each case the rear vortex is fed with hotter liquid metal coming from the laser spot area and colder one coming along the pool edge as previously observed in Fig. 14. These hotter and colder fluid streams mix while rotating counterclockwise towards the centre of the vortex. The fluid is then transported downwards from the vortex centre to feed the thermocapillary flow from below in the beam spot area. The transverse swirling structure indicated with a dotted arrow for C1 is instead along the travel direction with C2, as expected for a spot profile rotated by π rad. With the beam profile C3 a mixed pattern combining both transverse and longitudinal swirling structures can be seen, although shorter. The major difference between these three cases is the presence of a clockwise rotating fluid noticed earlier at the front of the pool with C2. This second vortex, absent for C1 and C3, is fed with hot fluid convected from the $\pi/4$ -front sector of the laser spot area by the thermocapillary flow. The front vortex is much closer to the beam spot than the rear vortex. The cooling along this front fluid flow is thus lower. At $U_{\text{laser}} = 5$ mm/s, the fluid entering the front vortex is at a temperature that is about 500 K higher than the fluid entering the rear vortex. As it exits the front vortex, it can be seen that the fused alloy flows back towards the bottom of the pool in the laser spot area before rising towards the melt surface.

5.4. Effect of beam shapes C1 to C3 on melt pool - discussion

The results confirming former knowledge were indicated above and are not repeated here. The discussion addresses first the possible effect of modelling simplifications on the computed results. The simulation model applied in this study already includes important elements such as free surface deformation, temperature dependent capillary and thermocapillary forces as well as temperature dependent thermodynamic and transport properties. Besides, the highest maximum temperature computed among all the test cases of this study was 3205 K. It was reached with the beam profile C3 and the laser travel speed $U_{\text{laser}} = 5$ mm/s. As this extremum is well below the boiling point of Ti-6Al-4V ($=3563$ K [15]), it corroborates that it was justified to neglect metal vaporisation. On the other hand, it is foreseen that a simplification that could matter in this study is the assumption of constant absorptivity. Absorptivity indeed depends on both the surface local temperature and the local angle of incidence of the beam as it strikes the surface. When the pool is fully developed, the local incidence at the beam spot center is 90° for both C2 and C3 (see Figs. 7 and 9) while the temperature is about 2600 K for C2 and 3000 K for C3 at $U_{\text{laser}} = 5$ mm/s (see Fig. 12). Applying the Drude model at normal incidence with the electric conductivity measured by Boivineau et al. [25] for Ti-6Al-4V and a beam wavelength of $1.06 \mu\text{m}$, the difference in absorptivity between C2 and C3 at the beam spot center turns out to be less than 1.2%. Considering now the outer part of the beam spot area, temperature and deviation of the beam incidence angle compared to normal incidence are $T \approx 2300$ K and $\theta \approx 20$ to 25° for C2 and $T \approx 2600$ K and $\theta \approx 30$ to 35° for C3. Applying now the Drude model combined with Fresnel's law, the difference in absorptivity between C2 and C3 at the beam spot outer edge is less than 2% at $U_{\text{laser}} = 5$ mm/s. However, these simple evaluations might underestimate the difference since they are based on computational results obtained with a constant absorptivity while the laser-metal fusion process is typically non-linear. Furthermore, the absorptivity is also expected to change with the travel speed due to the change in interaction time this implies. Considering the major role of the absorptivity, a more advanced evaluation of its effect would thus be of interest in a future study.

The second point discussed is the effect of changing the orientation of the Gaussian-elliptical beam profile. The results of section 5.3 did show

that the liquid alloy velocities computed for C1 and C2 are significantly larger than the travel speed and primarily governed by the temperature gradients generated by the beam profiles. If it could imply that heat transfer is essentially governed by heat conduction, the melt pools would reproduce each other by rotation in the same way as their respective power density distributions. Then, the volumes of the melt pools produced with C1 and C2 would be the same, and the conjecture made by Ayoola et al. [10] would be confirmed. But the fact that the process is governed by temperature gradients is not sufficient for heat transfer to behave as heat conduction since heat transfer within the pool is governed by convection which, in addition, is essentially non-linear (see e.g. Ref. [35] and references therein). With the process parameters of this study all the results (velocity and temperature fields, pool dimensions and volume) show that while C1 and C2 can be interchanged through a π -rotation about the beam axis, their pools do not preserve this property. According to the computational results, this is very probably related to the transverse narrowness of the pool formed with C2 that modifies the flow (compared to a π -rotated pool C1) in at least two ways. First, it accelerates the liquid alloy at the pool rear while pushing it ahead towards the beam spot area. And second, it re-directs the liquid alloy confined in the narrow pool front area through the front vortex towards the beam spot area. An important effect of this flow pattern specific to the beam profile C2 is that part of the hotter fluid recirculates within the hotter region of the pool through the front vortex rather than being convected along the colder mushy zone region where thermal energy is dissipated to the heat affected zone. Thus the 200 K higher temperature at the pool surface with the beam profile C2 compared to C1, while the power density distributions of these two cases have the same intensity and sharpness. This hot fluid re-circulation assists the fusion process through pre-heating the alloy located ahead of the laser spot centre, and feeds the laser spot area with re-circulated fluid metal that is less cooled than for the other profiles. The pre-heating is also observed to be more effective at low welding travel speed, that is at high interaction time. When the welding travel speed increases, the melt pool length decreases; accordingly, the distance over which the pre-heating takes place decreases and then its efficiency.

Next, the effect on the pool of the sharp Gaussian beam power density distribution C3 versus its transform C2 by elongation along the travel direction, is discussed. The beam spot C2 is almost 4-times longer than C3. The fact that the pool is longer with C2 than with C3 is certainly a straightforward consequence of the beam shapes. The beam spot C2 is as wide as C3; it corresponds to the same total laser power as C3 but its power density P_d is almost 4-times lower. C2 leads as expected to lower temperature and velocity induced by the thermocapillary acceleration at the outer edge of the beam spot than C3, with $T \approx 2300$ K and $U \approx 0.22$ m/s while $T \approx 2600$ K and $U \approx 0.38$ m/s for C3 (see Figs. 12 and 13). It implies that C2 results in a clearly lower lateral rate of convective heat transfer than C3 that certainly causes its smaller width. If the large major to minor axis ratio of the elliptical beam profile was lowered, the differences in P_d between the Gaussian-elliptical and the Gaussian profiles would diminish. Then, the differences in convective heat transfer would blur, and the pool widths would tend towards closer values, as observed experimentally by Ayoola et al. [10] with the much smaller elliptical aspect ratio.

The penetration depth and the pool volume obtained with C2 compared to C3 can hardly be simply motivated by the temperature gradients in the beam spot area. Especially since they become significantly larger with C2 than with C3 at low travel speed while P_d and the beam spot aspect ratio are kept unchanged. The computed velocity and temperature fields suggest that this non-linear effect of the beam shape on the melt pool depth and volume is also very probably due to the front vortex that is only formed with C2 and the related pre-heating effect of the high-temperature circulation flow between front vortex and beam spot area. The fact that the extent of the pre-heating shrinks when the travel speed is increased appears to support this explanation. The results suggest also that, with the process conditions of this study, there is a

threshold interaction time above which the pre-heating of case C2 becomes more effective than the sharpness of the beam profile C3 for promoting conversion of the laser energy entering the workpiece into latent heat of fusion rather than sensible enthalpy. This threshold corresponds here to a welding travel speed within the range $5 < U_{\text{laser}} < 7.5$ mm/s. It is likely that this threshold depends on the aspect ratio of the elongated beam spot profile. Besides, the closer isotherms observed at the travel speed of 5 mm/s in the HAZ behind the melt pool for case C2 compared to the other cases in Fig. 12 is here a consequence of the larger pool volume. A melt pool volume 30 % larger with C2 than with C3 indeed means that a larger fraction of the laser energy entering the workpiece is used as latent heat to fuse the alloy with C2 compared to C3. Therefore, a lower fraction of sensible energy remains to be conducted in the heat affected zone, thus the shorter distance needed for its dissipation.

Finally, when elongating the beam spot along the travel direction it can be seen in Fig. 8 (C3 to C2) that the melt pool width is lowered while no noticeable change in the width was detected in the experimental study of Ayoola et al. [10]. The process conditions of these two studies differ in three important aspects that are now examined to analyse possible reasons for these different responses. In this study the beam axis is almost at normal incidence for both C2 and C3 (see section 2) while in Ref. [10] the laser head was inclined at 45° against the vertical direction to produce the Gaussian-elliptic profiles. The deformation of the free surface was not documented in Ref. [10]. Nevertheless, assuming that it did not exceed 30° in the spot area, which can be reasonable as the fusion process was in conduction mode, the beam angle against the local normal to the melt pool surface was most probably still below the Brewster angle [36]. It is also assumed that the beam was unpolarized, as often the case for this type of application. Then, referring to the available absorption coefficient for iron provided as a function of the incidence angle by Dausinger and Shen [36], it might be extrapolated that the absorptivity did not change drastically when inclining the beam. Unfortunately, too little data is available to analyse further this point.

A second difference between the two studies comes from the material composition, in particular the amount of surfactant. With Ti-6Al-4V in argon atmosphere as in this study the amount of surfactant is negligible. On the other hand, the mild steel alloy S275 used in Ref. [10] can contain as much as 0.05 % in weight sulfur. According to the studies of Sahoo et al. [37] and Pitscheneder et al. [38] it is known that this is far beyond the amount necessary to change the direction of the thermocapillary force at the outer region of the pool surface, thus creating an inward counter flow that limits the lateral expansion of the melt pool. Therefore, although the exact amount of sulfur in the S275-material used in Ref. [10] is not documented, the presence of surfactant might contribute in explaining the different responses of the pool width observed in these two studies. However, the effect of the fraction of surfactant on the melt pool response to beam shaping is still little reported.

The third difference is the elliptical spot aspect ratio (r_{\parallel}/r_{\perp}) that is almost 4 in this study and only 1.4 in Ref. [10]. As a result, when deforming the beam shape from circular (reference) to elongated along the travel direction, the peak intensity is reduced to 25% of the reference value in this study while the reduction is only to 70% in Ref. [10]. It implies lower change in temperature gradient for the beam spot distortion of [10] compared to this study, thus lower change in thermocapillary flow, and lower change in pool width. This is consistent with the trend observed. Other results presented by Ayoola et al. [10] support this explanation. These authors did also investigate the effect of defocusing circular beam shapes of same nominal diameter for two different conditions. When switching from defocused (used as reference for this discussion) to focussed beam spot, the peak intensity was reduced to 60% of the reference value in one case and to 54% in the other case. The resultant effect on the pool width was not visible in the former case and less than 1 mm in the latter one. It seems to indicate that a rather large threshold in peak intensity change needs to be exceeded to

observe an effect on the pool width. Thus, the peak intensity reduction to 70% of the reference value made when elongating the circular beam shape was most probably below that threshold, which explains the negligible effect on the pool width observed in Ref. [10].

6. Conclusions

The influence of beam shaping was studied using a computational fluid dynamic approach. First of all, it is recommended to track the evolution of the melt pool volume when seeking (numerically) for quasi-steady process conditions, since the liquid volume fraction or α -field can require more time to fully develop than the other fields.

The effect of three beam shapes on the melt thermal flow was investigated. These shapes were a Gaussian profile and its transverse and longitudinal elliptic elongations with an aspect ratio of almost 4. It was verified that beam elongation, which scales down the integrated laser spot power density, lowers the temperature gradients, weakens the thermocapillary flow, and smooths the deformation (waviness) of the free surface. Furthermore, it was found that

- (1) The three beam shapes studied induce melt flow patterns with distinctive specificities that are not all linearly related to the temperature gradients even if the welding travel speed is small compared to the melt velocity induced by the temperature gradients.
- (2) While they have the same transverse radius, the Gaussian profile leads to wider pool than its longitudinal elliptic elongation for the large ellipse-aspect ratio of this study.
- (3) While the transverse and longitudinal Gaussian-elliptic beam profiles can be obtained from each other by rotation, their pools (both flow pattern and geometry) cannot, although the welding travel speed is small compared to the melt velocity induced by the temperature gradients. Moreover, their pool volumes differ significantly.
- (4) The profile elongated along the welding travel direction confines in a narrow pool front area the thermocapillary flow thus inducing a vortex at each side (by symmetry) of the pool front. This vortex assists the fusion process through pre-heating the alloy, and enhances both penetration depth and fused volume. As a counterpart it lowers the amount of thermal energy dissipated in the heat affected zone. These effects are more pronounced at low welding travel speed at which they can compete with or even outdo the large penetration depth characteristic of the Gaussian profile with integrated laser spot power density four times larger.

Melt heat convection has thus a leading order role when studying the effect of beam shaping, even if melt velocity induced by the temperature gradients is significantly larger than the travel speed. It implies that mastering the effect of beam shaping on the melt heat convection is a key element for designing and optimizing a beam for a specified pre-welding joint geometry as well as for requirement on the resulting weld seam quality.

Declaration of competing interest

The authors declare that they have no known competing financial interests or personal relationships that could have appeared to influence the work reported in this paper.

Data availability

Data will be made available on request.

Acknowledgement

This research work is supported by grants from the Swedish

Knowledge Foundation, projects AdOpt (20170315) and SAMw (20170060), which is gratefully acknowledged. The authors would also like to thank Dr. Morgan Nilsen for his technical support during experiments and PhD-student Karthikeyan Thalavai Pandian for his support in preparing the cross-cut images of the welds.

References

- [1] G.G. Gladush, I. Smurov, *Physics of Laser Materials Processing - Theory and Experiment*, Springer, New York, 2011.
- [2] E. Assuncao, S. Williams, D. Yapp, Interaction time and beam diameter effects on the conduction mode limit, *Opt Laser. Eng.* 50 (2012) 823–828.
- [3] B. Victor, *Custom Beam Shaping for High-Power Fiber Laser Welding* PhD. Thesis, The Ohio State University, 2009.
- [4] A. Heralic, *Towards Full Automation of Robotized Laser Metal-Wire Deposition*. PhD Thesis, Chalmers University of Technology, 2009.
- [5] K.S. Hansen, M. Kristiansen, F.O. Olsena, Beam shaping to control of weld pool size in width and depth, *Phys. Procedia* 56 (2014) 467–476.
- [6] N. Kumar, M. Mukherjee, A. Bandyopadhyay, Study on laser welding of austenitic stainless steel by varying incident angle of pulsed laser beam, *Opt Laser. Technol.* 94 (2017) 296–309.
- [7] S. Kuryntsev, D. Kolesnikov, M. Vulpe, Investigation of the effect of welding heat input and focal distance of laser beam on penetration depth and dynamics of welding pool using a high-speed video camera, *Mater. Sci. Forum* 989 (2020) 721–732.
- [8] P. Li, Z. Lei, X. Zhang, J. Liu, Y. Chen, Effects of laser power on the interfacial intermetallic compounds and mechanical properties of dual-spot laser welded-brazed Ti/Al butt joint, *Opt Laser. Technol.* 124 (2020) 105987.
- [9] C.M. Tsai, C.K. Wu, Freeform lens design of beam shaping with user-defined rotation-symmetric profile by using numerical method, *IEEE Photon. J.* 11 (2019) 3, 1502812.
- [10] W.A. Ayoola, W.J. Suder, S.W. Williams, Effect of beam shape and spatial energy distribution on weld bead geometry in conduction welding, *Opt Laser. Technol.* 117 (2019) 280–287.
- [11] M. Rasch, C. Roider, S. Kohl, J. Strauß, N. Maurer, K.Y. Nagulin, M. Schmidt, Shaped laser beam profiles for heat conduction welding of Aluminium-Copper alloys, *Opt Laser. Eng.* 115 (2019) 179–189.
- [12] J. Sundqvist, A.F.H. Kaplan, L. Shachaf, A. Brodsky, C.J. Kong, J. Blackburn, E. Assuncao, L. Quintino, Numerical optimization approaches of single-pulse conduction laser welding by beam shape tailoring, *Opt Laser. Eng.* 79 (2016) 48–54.
- [13] J. Svenungsson, I. Choquet, A.F.H. Kaplan, Laser welding process - a review of keyhole welding modelling, *Phys. Procedia* 78 (2015) 182–191.
- [14] J. Cho, D.F. Farson, K.J. Hollis, J.O. Milewski, Numerical analysis of weld pool oscillations in laser welding, *J. Mech. Sci. Technol.* 29 (4) (2015) 1715–1722.
- [15] K.C. Mills, *Recommended Values of Thermophysical Properties for Selected Commercial Alloys*, Woodhead Publishing, 2002.
- [16] Y.-D. Kim, W.-S. Kim, A numerical analysis of heat and fluid flow with a deformable curved free surface in a laser melting process, *Int. J. Heat Fluid Flow* 29 (5) (2008) 1481–1493.
- [17] Z.S. Saldi, *Marangoni Driven Free Surface Flows in Liquid Weld Pools*. PhD Thesis, Delft University of Technology, 2012.
- [18] A. Ebrahimi, C.R. Kleijn, I.M. Richardson, The influence of surface deformation on thermocapillary flow instabilities in low Prandtl melting pools with surfactants, in: *Proceedings of the 5th World Congress on Mechanical, Chemical, and Material Engineering (MCM'19)* Lisbon, Portugal, HTFF, 201, 2019.
- [19] A.A. Bhatti, Z. Barsoum, H. Murakawa, I. Barsoum, Influence of thermo-mechanical material properties of different steel grades on welding residual stresses and angular distortion, *Mater. Des.* 6 (2015) 878–889.
- [20] C.W. Hirt, B.D. Nichols, Volume of fluid (VOF) method for the dynamics of free boundaries, *J. Comput. Phys.* 39 (1) (1981) 201–225.
- [21] O. Ubbink, *Numerical Prediction of Two Fluid Systems with Sharp Interfaces*. PhD Thesis, Imperial College, University of London, 1997.
- [22] J.U. Brackbill, D.B. Kothe, C. Zemach, A continuum method for modeling surface tension, *J. Comput. Phys.* 100 (2) (1992) 335–354.
- [23] A. Singh, R. Pardeshi, B. Basu, Modelling of convection during solidification of metal and alloys, *Sadhana* 26 (2001) 139–162.
- [24] F. Rösler, D. Brüggemann, Shell-and-tube type latent heat thermal energy storage: numerical analysis and comparison with experiments, *Heat Mass Tran.* 47 (2011) 1027–1033.
- [25] M. Boivineau, C. Cagran, D. Doytier, V. Eyraud, M.H. Nadal, B. Wilthan, G. Pottlacher, Thermophysical properties of solid and liquid Ti-6Al-4V (Ta6V) alloy, *Int. J. Thermophys.* 27 (2006) 507–529.
- [26] R. Rai, P. Burgardt, J.O. Milewski, T.J. Lienert, T. DebRoy, Heat transfer and fluid flow during electron beam welding of 21Cr-6Ni-9Mn steel and Ti-6Al-4V alloy, *J. Phys. Appl. Phys.* 42 (2009), 025503.
- [27] Z. Fan, *Numerical Modeling of Heat Transfer and Fluid Flow in Laser Metal Deposition by Powder Injection*. PhD. Thesis, Missouri University of Science and Technology, 2013.
- [28] M. Akbari, S. Saedodin, D. Toghraie, R. Shoja-Razavi, F. Kowsari, Experimental and numerical investigation of temperature distribution and melt pool geometry during pulsed laser welding of Ti-6Al-4V alloy, *Opt Laser. Technol.* 59 (2014) 52–59.
- [29] Y.A. Çengel, *Heat and Mass Transfer: A Practical Approach* (SI Units), third ed., McGraw Hill, 2007.
- [30] H.G. Weller, G. Tabor, H. Jasak, C. Fureby, A tensorial approach to computational continuum mechanics using object-oriented techniques, *Comput. Phys.* 12 (6) (1998) 620–631.
- [31] M. Shams, A.Q. Raeni, M.J. Blunt, B. Bijeljic, A numerical model of two-phase flow at the micro-scale using the volume-of-fluid method, *J. Comput. Phys.* 357 (2018) 159–182.
- [32] S.M.A. Noori Rahim Abadi, F. Sikström, A. Ancona, I. Choquet, Effect of Laser Energy Absorptivity Modelling on Melt Pool Geometry Preprint, 2021.
- [33] W.A. Ayoola, W.J. Suder, S.W. Williams, Parameters controlling weld bead profile in conduction laser welding, *J. Mater. Process. Technol.* 249 (2017) 522–530.
- [34] L. Aucott, H. Dong, W. Mirihanage, R. Atwood, A. Kidess, S. Gao, S. Wen, J. Marsden, S. Feng, M. Tong, T. Connolley, M. Drakopoulos, C.R. Kleijn, I. M. Richardson, D.J. Browne, R.H. Mathiesen, H.V. Atkinson, Revealing internal flow behaviour in arc welding and additive manufacturing of metals, *Nat. Commun.* 9 (2018) 1–7.
- [35] C. Chan, J. Mazumder, M. M Chen, A two-dimensional transient model for convection in laser melted pool, *Metall. Trans. A* 15 (12) (1984) 2175–2184.
- [36] F. Dausinger, J. Shen, Energy coupling efficiency in laser surface treatment, *ISIJ Int.* 33 (9) (1993) 925–933.
- [37] R. Sahoo, T. DebRoy, M.J. McNallan, *Metall. Trans. B* 19B (1988) 483–491.
- [38] W. Pitscheneder, T. DebRoy, K. Mundra, R. Ebner, Role of sulfur and processing variables on the temporal evolution of weld pool geometry during multi-kilowatt laser beam welding of steels welding, *Journal* 75 (1996) 3, 71s–80s.